Causality and double-negative metamaterials

Richard W. Ziolkowski* and Allison D. Kipple†
Department of Electrical and Computer Engineering, The University of Arizona, 1230 E. Speedway Boulevard, Tucson, Arizona 85721-0104, USA
(Received 9 May 2003; published 29 August 2003)

The causality of waves propagating in a double-negative (DNG) metamaterial ($\varepsilon_r<0$ and $\mu_r<0$) has been investigated both analytically and numerically. By considering the one-dimensional electromagnetic problem of a pulsed current sheet radiating into a DNG medium, it is shown that causality is maintained in the presence of a negative index of refraction only if the DNG medium is dispersive. A Drude model DNG medium is used in this study. Spectrograms of the wave phenomena in the dispersive DNG medium show that the higher frequency components, which create the leading edge of the electromagnetic signals and see a double positive (DPS) medium ($\varepsilon_r>0$ and $\mu_r>0$), arrive causally before the negative index effects germinate completely. Comparisons with approximate analytical results demonstrate the presence of the negative index of refraction properties in the continuous wave portion of the signals. This dynamic pulse reshaping between the positive and negative index of refraction wave components causes an apparent delay in the realization of the negative index of refraction properties. Pulse broadening of the signal tails is associated with both dispersion and a larger negative index of refraction seen by the associated wave components.

DOI: 10.1103/PhysRevE.68.026615 PACS number(s): 41.20.Jb, 42.25.Bs, 81.05.Zx, 03.50.De

I. INTRODUCTION

The index of refraction of a double-negative (DNG) metamaterial, i.e., a material with both negative permittivity and negative permeability (see, for instance, [1–4]), has been shown to be negative (see, for instance, [5–7]). There are now several theoretical and experimental studies that have been reported confirming this negative index of refraction (NIR) property and applications derived from it, such as phase compensation and electrically small resonators [8], negative angles of refraction [8–13], enhanced focusing [14–17], backward wave antennas [18], Čerenkov radiation [19], photon tunneling [20,21], and enhanced electrically small antennas [22]. These studies rely heavily on the concept that a continuous wave (CW) excitation of a DNG medium will lead to a NIR and, hence, to negative phase terms.

If one considers carefully the ramifications of a homogeneous, nondispersive DNG medium and the resulting NIR, one immediately encounters a paradox in the time domain. A source in such a DNG medium will generate a signal that propagates noncausally. On the other hand, many of the NIR studies have been based on numerical simulations in the time domain of dispersive DNG metamaterials. In fact, as shown in [5], realistic DNG metamaterials must be dispersive. How then does one reconcile the CW NIR properties associated with a nondispersive DNG medium with causal pulse propagation in a dispersive DNG medium? Can one rely on designs of NIR applications that rely on the CW behavior of the corresponding nondispersive DNG medium?

In this paper, the issue of causality in DNG metamaterials is considered by studying the one-dimensional electromagnetic problem of a pulsed source in a DNG medium. A lossy, dispersive Drude model is used to create the DNG medium. A finite difference time domain (FDTD) numerical solution of the problem is obtained. The source is driven by an excitation pulse that is based on a sinusoid and a smooth envelope. It is demonstrated that both the expected causal propagation and the NIR effects are obtained. Other recent considerations of causality (e.g., [13,23]) have, in effect, been limited to narrow bandwidth considerations. The corresponding nondispersive DNG medium problem is then considered. It is demonstrated analytically that only a noncausal exact solution exists. The noncausal analytical DNG solution and the causal FDTD DNG results are then reconciled by the presence of dispersion. It is shown that the leading edge of the pulse, which is associated with high frequencies, propagates causally in a double-positive (DPS) medium (i.e., a normal medium that has both positive permittivity and positive permeability), while the CW portion of the pulse senses the DNG medium and exhibits the NIR effects. The slower speed components appear to accumulate in the trailing edge. Both the leading and trailing edges of the pulse are shown to be strongly affected by the presence of dispersion. Using the nondispersive results to guide the construction of approximate solutions to the dispersive DNG medium problem, it is shown that the NIR effects obtained for the dispersive case coincide with those predicted by the nondispersive case. It is also shown that observed time delays in the realization of the NIR properties are directly associated with the transition from the causal DPS response to the DNG one. These observations reinforce the fact that DNG metamaterials and the associated NIR results are physical and that their experimental confirmation is consistent with the underlying wave propagation physics.

II. 1D-FDTD SIMULATOR

A one-dimensional FDTD simulation environment was utilized to study the characteristics of signals produced by a pulsed source in a DNG medium. This one-dimensional en-

*Email address: ziolkowski@ece.arizona.edu
†Email address: kipplea@ece.arizona.edu

vironment was convenient and incorporated all of the necessary physics. The field components were assumed to be E_x and H_y with the direction of propagation taken along the z axis. An electric current plane-wave source was located in the plane $z=0$, at the center of a very large DNG slab. The DNG slab was surrounded by free space and was centered in the FDTD domain. This slab geometry was used in order that standard, exact absorbing boundary conditions could be applied at the edges of the FDTD simulation space. The problem geometry is shown in Fig. 1.

As in [6], lossy Drude polarization and magnetization models were used to simulate the DNG medium. In the frequency domain, assuming an $\exp(-i\omega t)$ time dependence, this means the permittivity and permeability were described as

$$\varepsilon(\omega)=\varepsilon_0\left(1-\frac{\omega_{pe}^2}{\omega(\omega+i\Gamma_e)}\right),$$

$$\mu(\omega)=\mu_0\left(1-\frac{\omega_{pm}^2}{\omega(\omega+i\Gamma_m)}\right). \tag{1}$$

The corresponding time-domain equations for the polarization, P_x, and the normalized magnetization, $M_{ny}=M_y/\mu_0$, fields were

$$\partial_t^2 P_x+\Gamma_e\partial_t P_x=\varepsilon_0\omega_{pe}^2 E_x,$$

$$\partial_t^2 M_{ny}+\Gamma_m\partial_t M_{ny}=\mu_0\omega_{pm}^2 H_y. \tag{2}$$

The normalized magnetization was introduced to make the electric and magnetic field equations completely symmetric. By introducing the induced electric and magnetic currents

$$J_x=\partial_t P_x,$$

$$K_y=\partial_t M_{ny}, \tag{3}$$

and the source current, J_s, the field and current equations used to model the waves generated by a pulsed source in a DNG medium became

$$\partial_t E_x=-\frac{1}{\varepsilon_0}(\partial_z H_y+J_x+J_s),$$

$$\partial_t J_x+\Gamma_e J_x=\varepsilon_0\omega_{pe}^2 E_x,$$

$$\partial_t H_y=-\frac{1}{\mu_0}(\partial_z E_x+K_y),$$

$$\partial_t K_y+\Gamma_m K_y=\mu_0\omega_{pm}^2 H_y. \tag{4}$$

A lossless, nondispersive DPS medium was used as a comparison case. In such a DPS medium, the corresponding field and current equation set was simply

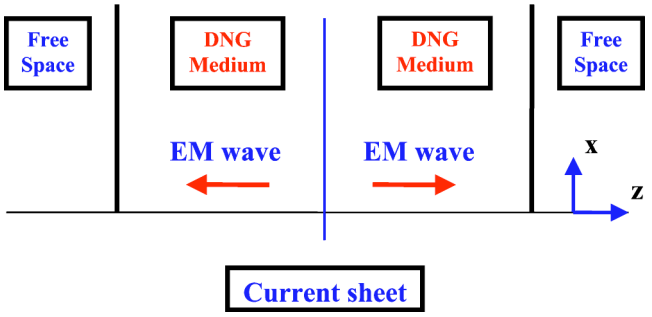

FIG. 1. (Color online) Configuration of the one-dimensional electromagnetic current sheet problem.

$$\partial_t E_x=-\frac{1}{\varepsilon_0}(\partial_z H_y+J_s),$$

$$\partial_t H_y=-\frac{1}{\mu_0}\partial_z E_x. \tag{5}$$

Equation sets (4) and (5) were solved self-consistently and numerically with the FDTD approach [24,25], i.e., these equations were discretized with a standard leap-frog in time, staggered grid approach. The electric field component was taken at the cell edges for integer time steps; the magnetic field components were taken at the cell centers for half-integer time steps. The electric and magnetic currents were located in space at the cell centers, and their time assignments were opposite to the corresponding electric and magnetic field components, i.e., the magnetic current components were sampled at integer time steps and the electric current component was sampled at half-integer time steps. This allowed a FDTD stencil that properly simulated matched medium conditions. The time step was set at 0.95 of the Courant value, i.e., $\Delta t=0.95\Delta z/c$.

In all cases, the center frequency of interest was chosen to be $f_0\equiv\omega_0/2\pi=30$ GHz, corresponding to a free-space wavelength $\lambda_0=1.0$ cm. Only matched media at f_0 were considered, i.e.,

$$Z(\omega_0)=\sqrt{\frac{\mu(\omega_0)}{\varepsilon(\omega_0)}}=\sqrt{\frac{\mu_0}{\varepsilon_0}}=Z_0. \tag{6}$$

Matching was obtained by setting the parameters for the electric and magnetic Drude models to be identical, i.e., $\omega_{pe}=\omega_{pm}=\omega_p$ and $\Gamma_e=\Gamma_m=\Gamma$. In all cases, only low loss values were considered by setting $\Gamma=10^{+8}=5.31\times10^{-4}\omega_0$. This value was selected to connect these results to those presented in [6] and [12]. A DNG medium matched to free space at $f_0=30$ GHz was considered, i.e.,

$$n(\omega_0)=\sqrt{\frac{\varepsilon(\omega_0)}{\varepsilon_0}}\sqrt{\frac{\mu(\omega_0)}{\mu_0}}=\sqrt{\varepsilon_r(\omega_0)}\sqrt{\mu_r(\omega_0)}=-1. \tag{7}$$

This required $\omega_p=2\pi\sqrt{2}\,f_0=2.66573\times10^{11}$ and, hence, $\Gamma=3.75\times10^{-4}\omega_p$.

The source was given by the expression

$$\vec{J}(z)=J_s(z)\hat{x}=-\delta(z)S(t)\hat{x}. \tag{8}$$

It was modeled in the FDTD simulation space by introducing the equivalent source $J_s\hat{x}=\hat{z}\times H_y\hat{y}$, i.e., $H_{y,\text{source}}=S(t)$ at the source plane. The input time signal was causal and was defined by

$$S(t)=g(t)\sin(\omega_0 t), \tag{9}$$

where the multiple cycle *m*-*n*-*m* envelope is given by the expression

$$g(t)=\begin{cases} 0 & \text{for } t<0 \\ g_{\text{on}}(t) & \text{for } 0\leqslant t<mT_p \\ 1 & \text{for } mT_p\leqslant t<(m+n)T_p \\ g_{\text{off}}(t) & \text{for } (m+n)T_p\leqslant t<(m+n+m)T_p \\ 0 & \text{for } (m+n+m)T_p\leqslant t, \end{cases} \tag{10}$$

where the period $T_p=1/f_0$. With the terms $x_{\text{on}}(t)=t/(mT_p)$ and $x_{\text{off}}(t)=[t-(m+n)T_p]/(mT_p)$, the continuous, two derivative smooth functions g_{on} and g_{off} can be written as

$$g_{\text{on}}(t)=10x_{\text{on}}^3(t)-15x_{\text{on}}^4(t)+6x_{\text{on}}^5(t),$$

$$g_{\text{off}}(t)=1-[10x_{\text{off}}^3(t)-15x_{\text{off}}^4(t)+6x_{\text{off}}^5(t)]. \tag{11}$$

The function $g_{\text{on}}(t)$ goes smoothly from 0 to 1 in *m* periods; the function $g_{\text{off}}(t)$ goes smoothly from 1 to 0 in *m* periods. The function $f(t)$ thus turns on smoothly in *m* periods, maintains a constant amplitude for *n* periods, and turns off smoothly in *m* periods. The more cycles in the center portion, i.e., the larger *n* is, the narrower the bandwidth and the closer the input pulse is to a CW signal. The shorter the turn-on and turn-off sections are, i.e., the smaller *m* is, the broader the bandwidth is and, in particular, the more high frequency content there is in the pulse.

The simulation space was discretized into cells with a length $\Delta z=\lambda_0/100=100\ \mu$m. The FDTD predicted electric field values at $z=100\Delta z$ and $z=120\Delta z$ for a 5-10-5 input pulse in the dispersive DNG medium are shown in Fig. 2(a). An expanded view of the leading edge of these pulses is shown in Fig. 2(b). The corresponding FDTD predicted electric field values for a lossless nondispersive DPS medium with $n=+1$ are shown in Figs. 3(a) and 3(b). Comparing these sets of figures, one can clearly see that, as in the DPS case, the fronts of the signals in the DNG medium arrive causally at the observation points. In the DPS case, the peaks of the central, CW portion of the pulse observed at the more distant *point 2* occur *later* in time than they do at *point 1*. In contrast, one can see that in the DNG case the NIR effects (e.g., negative phase and phase velocity) evolve as the CW portion of the signal is realized, e.g., the peaks of the CW portion of the pulse observed at the more distant *point 2* occur *earlier* in time than they do at *point 1*. Dispersive effects are also apparent in the DNG results as the observation points move farther away from the source. These results are consistent with those reported in [6] for a DNG slab.

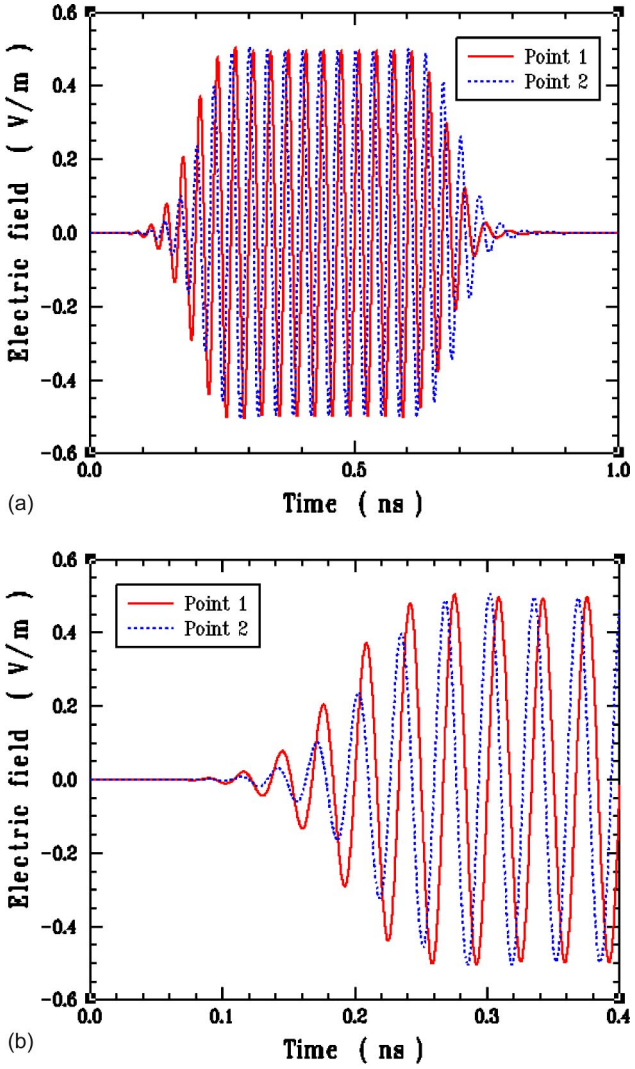

FIG. 2. (Color online) FDTD predicted electric field values in the DNG medium for the 5-10-5 input pulse (a) measured at the points $z=100\Delta z$ and $z=120\Delta z$ and (b) zoomed to the front of those pulses, where $\Delta z=100\ \mu$m.

III. ANALYTICAL CONSIDERATIONS

Consider now the plane-wave source in a hypothetical lossless, nondispersive DNG medium with $\varepsilon_r=\mu_r=-1$. The Maxwell equations become

$$\partial_t E_x=\frac{1}{|\varepsilon|}(\partial_z H_y+J_s),$$

$$\partial_t H_y=\frac{1}{|\mu|}\partial_z E_x. \tag{12}$$

First, let the excitation signal be given by the expression

$$S(t)=[H(t)-H(t-T)]\sin(\omega_0 t), \tag{13}$$

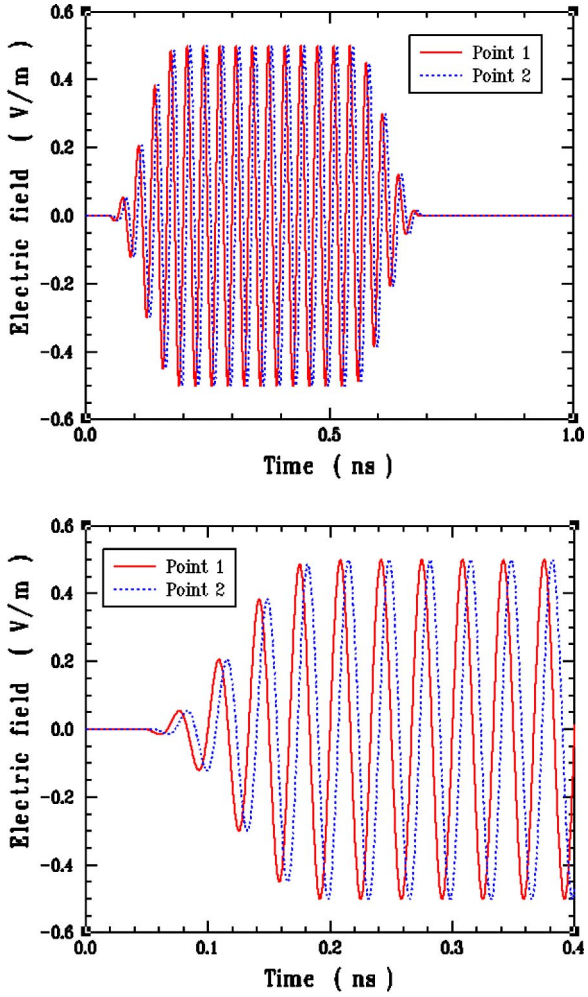

FIG. 3. (Color online) FDTD predicted electric field values in the DPS medium for the 5-10-5 input pulse (a) measured at the points $z=100\Delta z$ and $z=120\Delta z$ and (b) zoomed to the front of those pulses, where $\Delta z=100$ μm.

where $T=(m+n+m)T_p$ and the Heaviside function

$$H(t)=\begin{cases}0 & \text{for } t<0\\ 1 & \text{for } t\geqslant 0.\end{cases} \tag{14}$$

Introducing the variable

$$t_0=|\varepsilon||\mu||z|, \tag{15}$$

it is readily shown that the solution to Eqs. (12) and (13) is

$$E_x(z,t)=\frac{1}{2}\frac{|\mu|^{1/2}}{|\varepsilon|^{1/2}}[H(t+t_0)-H(t+t_0-T)]\sin[\omega_0(t+t_0)],$$

$$H_y(z,t)=\frac{1}{2}\mathrm{sgn}(z)[H(t+t_0)-H(t+t_0-T)]\times\sin[\omega_0(t+t_0)], \tag{16}$$

where

$$\mathrm{sgn}(z)=\begin{cases}-1 & \text{for } z<0\\ +1 & \text{for } z\geqslant 0.\end{cases} \tag{17}$$

We note for completeness that $\partial_z|z|=\mathrm{sgn}(z)$ and $\partial_z\,\mathrm{sgn}(z)=+2\delta(z)$.

The corresponding DPS medium results with $\varepsilon_r=\mu_r=+1$ are described by the Maxwell equations

$$\partial_t E_x=-\frac{1}{|\varepsilon|}(\partial_z H_y+J_s),$$

$$\partial_t H_y=-\frac{1}{|\mu|}\partial_z E_x, \tag{18}$$

and their solutions

$$E_x(z,t)=\frac{1}{2}\frac{|\mu|^{1/2}}{|\varepsilon|^{1/2}}\{H(t-t_0)-H[t-(t_0+T)]\}\times\sin[\omega_0(t-t_0)],$$

$$H_y(z,t)=\frac{1}{2}\mathrm{sgn}(z)\{H(t-t_0)-H[t-(t_0+T)]\}\times\sin[\omega_0(t-t_0)]. \tag{19}$$

Comparing the two results, Eqs. (16) and (19), one can clearly see that the lossless, nondispersive DNG medium solution is noncausal. This observation is in complete agreement with those made in [5].

Similarly, with the *m-n-m* excitation pulse given by Eq. (9), the DNG medium solution is

$$E_x(z,t)=\frac{1}{2}\frac{|\mu|^{1/2}}{|\varepsilon|^{1/2}}g(t+t_0)\sin[\omega_0(t+t_0)],$$

$$H_y(z,t)=\frac{1}{2}\mathrm{sgn}(z)g(t+t_0)\sin[\omega_0(t+t_0)], \tag{20}$$

and the DPS medium solution is

$$E_x(z,t)=\frac{1}{2}\frac{|\mu|^{1/2}}{|\varepsilon|^{1/2}}g(t-t_0)\sin[\omega_0(t-t_0)],$$

$$H_y(z,t)=\frac{1}{2}\mathrm{sgn}(z)g(t-t_0)\sin[\omega_0(t-t_0)]. \tag{21}$$

The DNG medium result is again noncausal while the DPS medium result is causal. The FDTD results shown in Fig. 3 recover the DPS solution (21) to within 0.1%.

Led by the observed combination of causal envelopes and NIR effects of the central portions of the DNG FDTD results, we consider the following approximate analytical solutions to the fields produced by the abrupt and smoothed windowed sine waveforms, respectively:

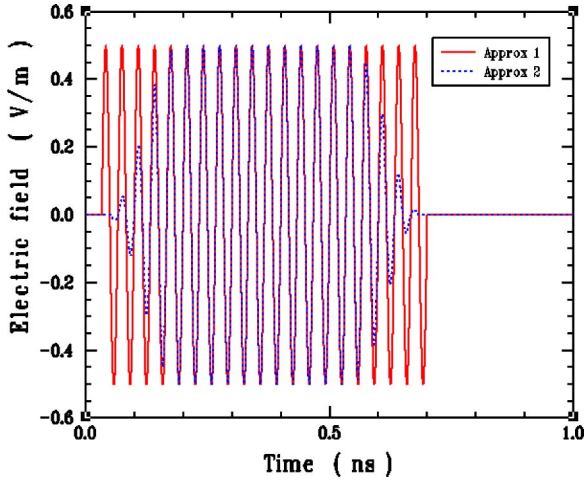

FIG. 4. (Color online) Approximate electric field values in the DNG medium for the 5-10-5 input pulse and $\Delta z = 100\ \mu$m measured at the point $z = 100\Delta z$.

$$E_x(z,t) = \frac{1}{2}\frac{|\mu|^{1/2}}{|\varepsilon|^{1/2}}\{H(t-t_0) - H[t-(t_0+T)]\} \times \sin[\omega_0(t+t_0)],$$

$$H_y(z,t) = \frac{1}{2}\mathrm{sgn}(z)\{H(t-t_0) - H[t-(t_0+T)]\} \times \sin[\omega_0(t+t_0)], \quad (22)$$

and

$$E_x(z,t) = \frac{1}{2}\frac{|\mu|^{1/2}}{|\varepsilon|^{1/2}} g(t-t_0)\sin[\omega_0(t+t_0)],$$

$$H_y(z,t) = \frac{1}{2}\mathrm{sgn}(z) g(t-t_0)\sin[\omega_0(t+t_0)]. \quad (23)$$

These solutions would allow for forward propagation in time while maintaining the solution's negative CW phase characteristics. Inserting the proposed solution (22) into Eqs. (12), one finds that it does not exactly solve them. The defects in this proposed solution occur as δ-function contributions at $t = t_0$ and $t = t_0 + T$. Similarly, inserting the proposed solution (23) into Eqs. (12), one finds that it also is not an exact solution and its failings as an exact solution occur as defects proportional to the derivatives of the turn-on and turn-off portions of the envelope function g. Note, however, that the CW portions of both of these proposed solutions do satisfy the Maxwell equations. Consequently, since the defects are highly localized, we will take Eqs. (22) and (23) as approximate solutions for the DNG case.

The electric field components of the approximate analytical solutions (22) and (23) for the 5-10-5 excitation pulse are compared at the point $z = 100\Delta z$ in Fig. 4. Approximation 1 denotes the electric field component given in Eqs. (22); approximation 2 denotes the electric field component given in Eqs. (23). Complete agreement of the CW portions of these results is observed, as expected. Their differences occur simply in how each of them is turned on and off. We note that the approximate solution (22) contains extremely high frequency content because of its abrupt turn-on and turn-off. The *n-m-n* form is more realistic and, as Fig. 4 shows, it contains the essential characteristics of this limiting case.

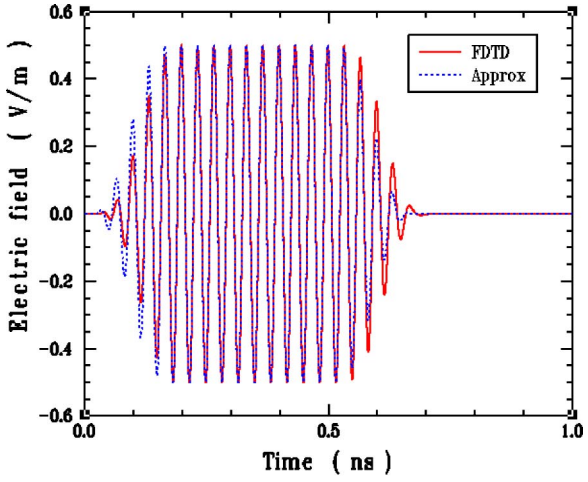

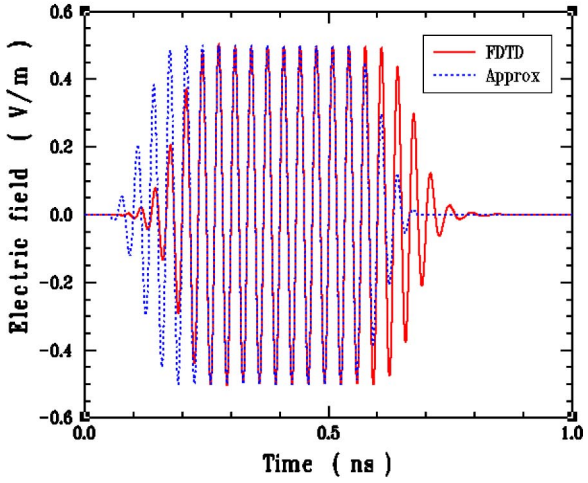

FIG. 5. (Color online) Comparison of the FDTD predicted and approximate analytical electric field values in the DNG medium for the 5-10-5 input pulse measured at the points (a) $z = 30\Delta z$ and (b) $z = 100\Delta z$, where $\Delta z = 100\ \mu$m.

The electric field component of the approximate solution given by Eqs. (23) for the 5-10-5 excitation pulse is compared to the corresponding FDTD results for the dispersive DNG medium at the points $z = 30\Delta z$ and at $z = 100\Delta z$ in Figs. 5(a) and 5(b), respectively. The corresponding results for a 2-16-2 excitation pulse were also obtained. Because the turn-on and turn-off portions of the 2-16-2 pulse are shorter, the time discretization was halved by decreasing the spatial discretization by a factor of 2 to $\Delta z' = 5.0 \times 10^{-5}$ m. The electric field component of the approximate solution given by Eqs. (23) for the 2-16-2 excitation pulse is compared to the FDTD result for the DNG medium at the points, $z = 60\Delta z'$ and $z = 200\Delta z'$, in Figs. 6(a) and 6(b), respectively. These observation points are located at the same distances away from the source, $z = 0.003$ m and $z = 0.01$ m, as they are for the 5-10-5 excitation pulse case.

From both sets of results, one can clearly discern the

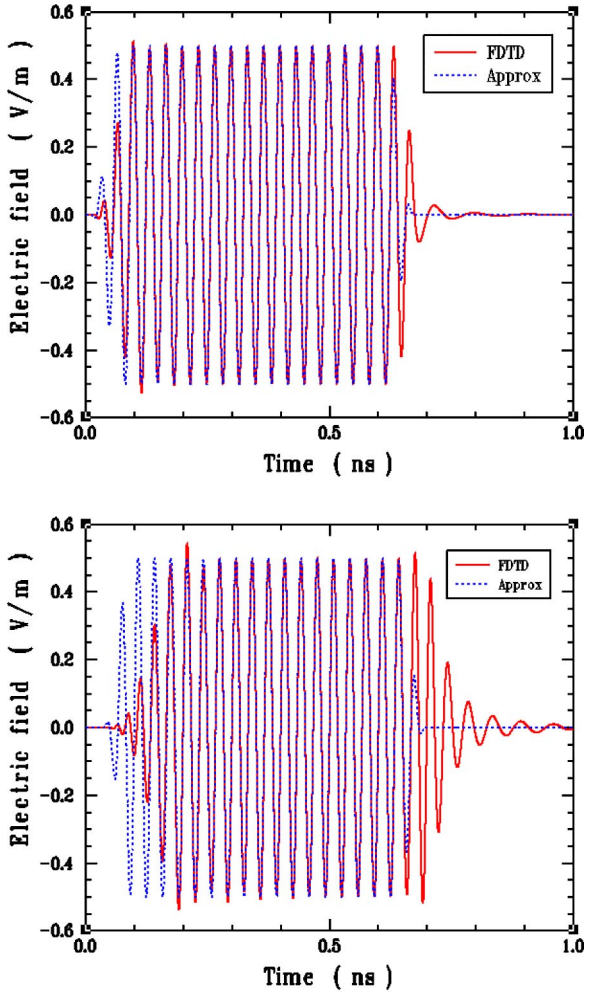

FIG. 6. (Color online) Comparison of the FDTD predicted and approximate analytical electric field values in the DNG medium for the 2-16-2 input pulse measured at the points (a) $z=60\Delta z'$ and (b) $z=200\Delta z'$, where $\Delta z'=50$ μm.

causal nature of the entire FDTD solution. One can also see that the NIR effects in the CW portions of the FDTD and the approximate results agree quite well. Thus, the NIR effects associated with a CW analysis are indeed recovered by the lossy, dispersive FDTD results. Clearly, if the loss were larger, the clarity of these CW components will be lost among the dispersive effects. This occurs even for the present cases as the observation points move much farther away from the source plane.

One can also immediately see from Figs. 5 and 6 that the main differences between the FDTD and the approximate results occur principally in the turn-on and turn-off portions of the envelope, as expected from the approximate solution analysis. The presence of dispersion is clearly seen in these regions. The faster turn-on envelope of the 2-16-2 pulse shows less dispersive effects than does the 5-10-5 excitation pulse. This might be expected since the turn-on portion of the envelope of the 2-16-2 pulse has higher frequency content than does the corresponding portions of the 5-10-5 envelope. Consequently, according to the Drude model, it sees a medium more like free space and less dispersion. On the other hand, there are larger differences in the turn-off portions of the 2-16-2 excitation pulse results than there are in those produced by the 5-10-5 excitation pulse. This trailing edge has more of its own higher and lower frequency components that are subject to dispersion; and it accumulates more of the slower moving, lower frequency components generated in the earlier portions of the pulse. Moreover, comparing the set of results at the point closer to the source with the one farther away from it, one observes that there are time delays between when the CW NIR effects are completely present and when they lose their dominance to the dispersive effects and that these delays increase as the observation point moves farther away from the source.

IV. SPECTROGRAM CONSIDERATIONS

How is it then that the dispersive effects reconcile the NIR and causal behaviors? To address this issue, we have studied spectrograms [26,27] of the source-generated pulse as it arrives at various observation points in the DNG medium. We recall that the magnitude of the phase and group speeds of the wave in the low loss limit are given, respectively, by the expressions

$$|v_p(\omega)| = \frac{c}{|\varepsilon_r|^{1/2}|\mu_r|^{1/2}} = \frac{c}{|1+\mathrm{Re}(\chi)|} \approx \frac{\omega^2}{|\omega^2-\omega_p^2|}c, \tag{24}$$

$$v_g(\omega) = \frac{c}{1+\mathrm{Re}(\chi)+\omega\partial_\omega[\mathrm{Re}(\chi)]} \approx \frac{\omega^2}{\omega^2+\omega_p^2}c, \tag{25}$$

where the real part of the susceptibility $\mathrm{Re}(\chi)=\mathrm{Re}[-\omega_p^2/\omega(\omega+i\Gamma)]\approx-\omega_p^2/\omega^2$. We also recall that the point in the frequency spectrum of the Drude model that isolates the DNG and the DPS regions occurs when $\varepsilon_r=\mu_r=0$, i.e., when $\omega=\omega_p$, hence when $f=\sqrt{2}\,f_0=42.42$ GHz. Well above this frequency, the permittivity and permeability are those of free space. Thus, the highest frequency components propagate causally in a medium that looks like free space. In particular, these components are the ones mainly responsible for the turn-on and turn-off portions of the envelope. The lower frequencies propagate with speeds slower than their value at the CW portion of the pulse, ω_0, i.e., $|v_p(\omega_0)| \approx c$.

To illustrate these effects, the spectrograms of the 1-1-1, 2-16-2, and 5-10-5 generated electric field pulses at $z=0.01$ m in the dispersive DNG medium were obtained. They are plotted in Figs. 7–9, respectively. The spectrograms were generated by taking Blackman-windowed Fourier transforms at every fourth sample in the signal data [26,27]. The number of signal samples analyzed by each transform was determined such that, after the data selection was windowed, the selection would represent at least a few and at most several wavelengths, depending on its frequency components. As a result, 512 signal samples were used in the transforms of the 5-10-5 pulse results, and 1024 signal samples were used in transforms of the 1-1-1 and 2-16-2 pulse results. Note that the spectrograms produced using a smaller signal slice in the Fourier transform became too noisy for interpretation, and larger signal slices resulted in

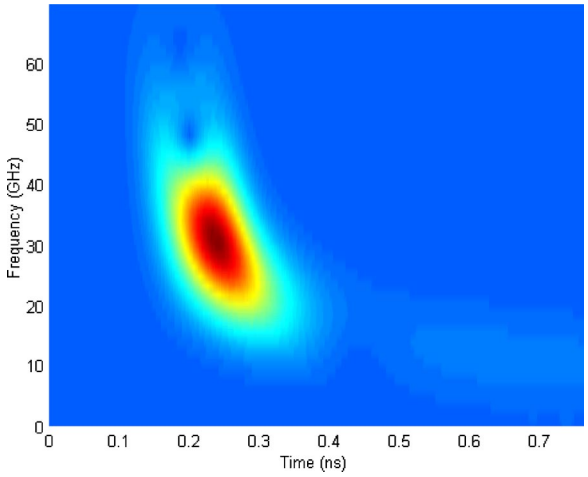

FIG. 7. (Color online) Spectrogram of the FDTD predicted field values in the DNG medium measured at the point $z=200\Delta z'$ for the 1-1-1 input pulse, where $\Delta z'=50$ μm.

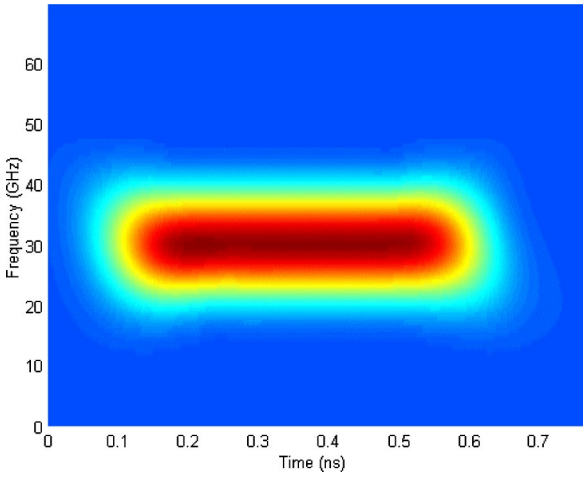

FIG. 9. (Color online) Spectrogram of the FDTD predicted field values in the DNG medium measured at the point $z=100\Delta z$ for the 5-10-5 input pulse, where $\Delta z=100$ μm.

broad areas in the spectrogram where the entire signal spectrum was displayed. The use of larger signal slices also shifted the estimates for the arrival times of various frequencies. The Fourier transforms were zero-padded to a size of 4096 to obtain sufficient resolution (<1 GHz sample spacing) near the center frequency (30 GHz) of the signals.

The resulting spectrograms shown in Figs. 7–9 then indicate, respectively, a good approximation of the frequency components present at the location $z=0.01$ m at various points in time for the 1-1-1, 2-16-2, and 5-10-5 cases. The three-cycle, 1-1-1 pulse spectrogram in Fig. 7 shows a negative slope. The higher frequencies propagate faster, hence they arrive sooner than the lower frequency components. While this behavior is present in the turn-on and turn-off portions of the results shown in Figs. 8 and 9, it is clearer in Fig. 8 since the 2-16-2 pulse has faster rates of change that are more closely related to the 1-1-1 case.

A plot of the Fourier transform output for data sections near the leading edge, central portion, and trailing edge of the FDTD DNG results for the 2-16-2 input pulse is shown in Fig. 10. All of the spectra are normalized to unity for comparison purposes. This figure clearly demonstrates that the leading edge of the pulse has significantly higher frequency content, the central portion of the pulse is dominated by the CW frequency, and the trailing edge of the pulse has significantly lower frequency content. Correlating this with Fig. 8, one then sees that those frequencies, hence the leading front of the pulse, arrive first to preserve causality.

To further investigate this dynamic pulse reshaping between the positive index of refraction (PIR) high frequency

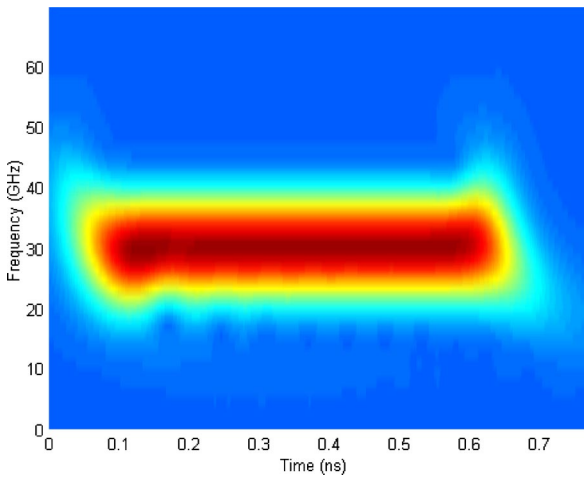

FIG. 8. (Color online) Spectrogram of the FDTD predicted field values in the DNG medium measured at the point $z=200\Delta z'$ for the 2-16-2 input pulse, where $\Delta z'=50$ μm.

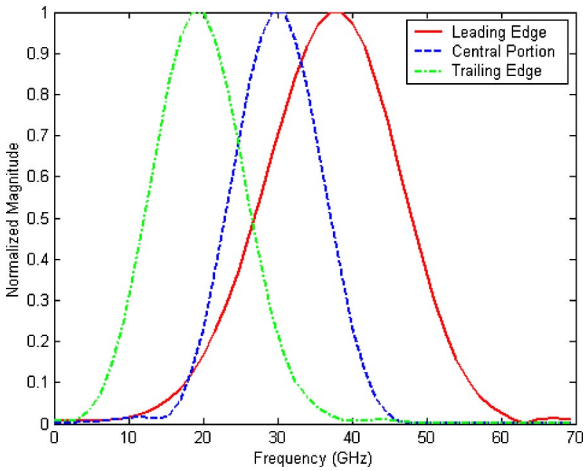

FIG. 10. (Color online) Normalized frequency composition of the (1) leading edge, (2) central portion, and (3) trailing edge of the DNG FDTD result measured at the point $z=200\Delta z'$ for the 2-16-2 input pulse, where $\Delta z'=50$ μm.

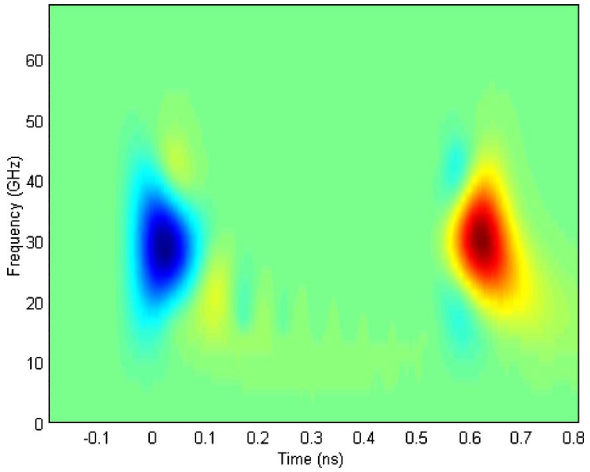

FIG. 11. (Color online) Spectrogram of the difference between the dispersive DNG 2-16-2 FDTD result shown in Fig. 8 and the corresponding approximate analytical solution. Red/dark region on the right (blue/dark region on the left) represents larger FDTD (approximate solution) values.

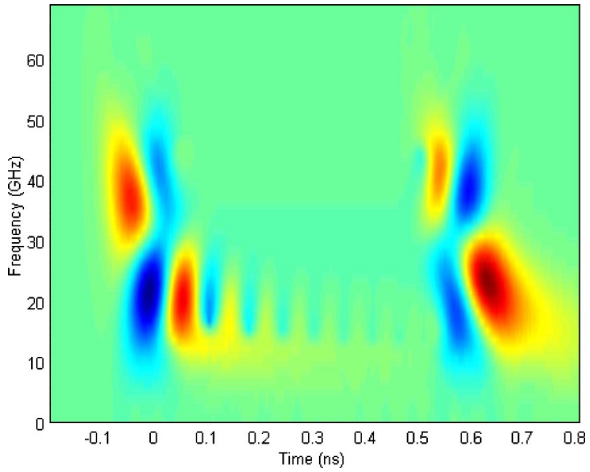

FIG. 12. (Color online) Spectrogram of the difference between the dispersive DNG 2-16-2 FDTD result shown in Fig. 8 and the corresponding approximate analytical solution when their CW portions are aligned. Red/dark region in the left-upper and right-lower portions of the left side and in the left-upper and right-lower portions of the right side of the figure represents larger FDTD values. Blue/dark region in the left-lower and right-upper portions of the left side and in the left-lower and right-upper portions of the right side of the figure represents larger approximate solution values.

components and the NIR center frequency and low frequency components, the differences between the spectrograms of the FDTD dispersive DNG results and the approximate solutions (23) were obtained. These spectrograms were also zero-padded at negative times to clarify the frequency components in the earliest portions of the signals. The 2-16-2 results measured at $z=0.01$ m are shown in Fig. 11. Although the FDTD DNG and the approximate solution signal fronts arrive at the same time and their CW portions are in very good agreement, the difference spectrograms filter out most of the CW behavior and reveal the importance of the apparent time delay and dispersive properties of the leading and trailing edges of the FDTD results. One finds that the CW portions of the FDTD results are not fully germinated until a time later than with the approximate solution. Similarly, the trailing edge of the FDTD result contains information that is delayed relative to the approximate solution. These delays reinforce similar observations made with regard to Figs. 5 and 6.

By aligning the CW portions of the FDTD and the approximate solution results and then generating the difference spectrogram, one can filter out all of the CW behavior and highlight the remaining low and high frequency behavior. The spectrogram for the 2-16-2 input pulse results measured at $z=0.01$ m is shown in Fig. 12. The transition from the off state to the CW state in the FDTD DNG data shows the necessary presence of higher frequency components very early in time to reconstruct the pulse front. The lower frequencies of the leading edge needed to complete the response in the DNG medium arrive later. This explains the slower turn-on of the FDTD results in comparison to the approximate solution. The trailing edge of the DNG FDTD result does contain significantly more of the lower frequency components while the presence of higher frequency components earlier in time aids the transition from the CW portion to the off state. This behavior adds delay to that already incurred with the turn-on portion of the pulse and explains the apparent lag in the turn-off of the FDTD results.

V. CONCLUSIONS

The one-dimensional electromagnetic problem of a current sheet source in a dispersive DNG medium was considered. A lossy Drude model of the DNG medium was used. The solution was generated numerically with the FDTD method. The analogous problem in a nondispersive DNG medium was also considered. It was shown that the solution to this problem is not causal in agreement with similar observations given in [5]. Approximate solutions that combined causal envelopes and the NIR properties of the nondispersive DNG medium were constructed; they were shown to compare well to the FDTD results for the dispersive DNG medium. It was thus demonstrated that causal results do indeed require the presence of dispersion in DNG media. Spectrograms of the FDTD results for the dispersive DNG medium and of the differences between those FDTD results and the approximate analytical solution revealed that the highest frequency components, which experience a DPS (PIR) medium, arrive first and are responsible for generating the front edge of the dispersive DNG pulse results. They also revealed that the trailing edge contained significant lower frequency components that see a DNG medium and have much slower wave speeds. The apparent delays in the germination of the CW portion of the pulse and in its termination were correlated with these dispersive effects. Thus, the dynamic reshaping of the DNG pulses occurs because of the different arrival times for the higher and lower frequency components.

It was also demonstrated that the CW portions of the

pulses do obey all of the NIR effects expected from a time-harmonic analysis in a nondispersive DNG medium. Thus, CW analyses of DNG media are credible as long as very narrow bandwidth pulse trains are considered for any practical realizations. This has been the case in all of the experimental results reported to date. Moreover, time delays for the realization of the NIR effects are inherent in the processes dictated by the dispersive nature of the physics governing them.

Even though the results presented here were derived for the broad bandwidth DNG Drude model, it is anticipated that the dynamic reshaping due to dispersive effects will also play a similar role in current metamaterial realizations of DNG media. This is particularly true of the planar implementations [15–18] that realize the Drude behavior. It should also be true for the nonplanar metamaterial constructs that involve highly resonant elements that achieve DNG properties in narrow frequency bands. In fact, this dynamic reshaping will occur at a faster rate since changes in the medium parameters from the DPS to the DNG states will be much more rapid. Furthermore, the dynamic reshaping must also occur at the interfaces between DPS and DNG media. The delays in the reflected pulse formation observed in [12] and [13] occur as the dispersive effects sort out the frequency components for the wavefronts and the appropriate propagation directions for the reflected and transmitted waves. Since most of the current nonplanar DNG metamaterial experiments are of the slab variety, these dynamic reshaping effects would be measurable if the experimental results were resolved in time.

It is interesting to note that the DNG results presented here can be related to Feynman's description of the interactions of electrons and positrons [28]. In particular, if one views the causal envelope propagating forward in time as an electron and the NIR CW wave propagating backward in time as a positron, then the positronlike CW wave is annihilated by the electronlike envelope at the pulse front. The scattered particle is the resulting wave that contains the NIR properties but is causal and propagating forward in time. The vertex interaction is smeared in time by the dispersive effects; it funnels the highest frequencies into the pulse front and properly distributes the higher and lower frequencies to provide the transition from the off-state to the CW on-state.

ACKNOWLEDGMENTS

This work was supported in part by DARPA under Contract No. MDA972-03-100.

[1] V. G. Veselago, Phys. Usp. **10**, 509 (1968).
[2] D. R. Smith, W. J. Padilla, D. C. Vier, S. C. Nemat-Nasser, and S. Schultz, Phys. Rev. Lett. **84**, 4184 (2000).
[3] R. A. Shelby, D. R. Smith, S. C. Nemat-Nasser, and S. Schultz, Appl. Phys. Lett. **78**, 489 (2001).
[4] R. W. Ziolkowski, IEEE Trans. Antennas Propag. **51**, 1516 (2003).
[5] D. R. Smith and N. Kroll, Phys. Rev. Lett. **85**, 2933 (2000).
[6] R. W. Ziolkowski and E. Heyman, Phys. Rev. E **64**, 056625 (2001).
[7] C. Caloz, C.-C. Chang, and T. Itoh, J. Appl. Phys. **90**, 5483 (2001).
[8] N. Engheta, Antennas Wireless Propagat. Lett. **1**, 10 (2002).
[9] A. Shelby, D. R. Smith, and S. Schultz, Science **292**, 77 (2001).
[10] J. A. Kong, B.-I. Wu, and Y. Zhang, Microwave Opt. Technol. Lett. **33**, 136 (2002).
[11] P. Kolinko and D. R. Smith, Opt. Express **11**, 640 (2003).
[12] R. W. Ziolkowski, Opt. Express **11**, 662 (2003).
[13] S. Foteinopoulou, E. N. Economou, and C. M. Soukoulis, Phys. Rev. Lett. **90**, 107402 (2003).
[14] J. B. Pendry, Phys. Rev. Lett. **85**, 3966 (2000).
[15] G. V. Eleftheriades, A. K. Iyer, and P. C. Kremer, IEEE Trans. Microwave Theory Tech. **50**, 2702 (2002).
[16] A. K. Iyer, P. C. Kremer, and G. V. Eleftheriades, Opt. Express **11**, 696 (2003).
[17] K. G. Balmain, A. A. E. Lüttgen, and P. C. Kremer, IEEE Antennas Wireless Propagat. Lett. **1**, 146 (2002).
[18] A. Grbic and G. V. Eleftheriades, J. Appl. Phys. **92**, 5930 (2002).
[19] J. Lu, T. M. Grzegorczyk, Y. Zhang, J. Pacheco, Jr., B.-I. Wu, J. A. Knog, and M. Chen, Opt. Express **11**, 723 (2003).
[20] Z. M. Zhang and C. J. Fu, Appl. Phys. Lett. **80**, 1097 (2002).
[21] L. Wu, S. He, and L. Chen, Opt. Express **11**, 1283 (2003).
[22] R. W. Ziolkowski and A. D. Kipple, IEEE Trans. Antennas Propagat., Special Issue on Metamaterials (to be published).
[23] J. Pacheco, Jr., T. M. Grzegorczyk, B.-I. Wu, Y. Zhang, and J. A. Kong, Phys. Rev. Lett. **89**, 257401 (2002).
[24] A. Taflove, *Computational Electrodynamics: The Finite-Difference Time-Domain Method* (Artech House, Inc., Norwood, MA, 1995).
[25] *Advances in Computational Electrodynamics: The Finite-Difference Time-Domain Method*, edited by A. Taflove (Artech House, Inc., Norwood, MA, 1998).
[26] R. S. Massey, S. O. Knox, R. C. Franz, D. N. Holden, and C. T. Rhodes, Radio Sci. **33**, 1739 (1998).
[27] A. V. Oppenheim and R. W. Schafer, *Discrete-Time Signal Processing*, 2nd ed. (Prentice Hall, Upper Saddle River, NJ, 1999).
[28] J. D. Bjorken and S. D. Drell, *Relativistic Quantum Mechanics* (McGraw Hill, New York, 1964), Chap. 5, pp. 63–75.